Materials Science & Engineering A 727 (2018) 123–132

Contents lists available at ScienceDirect

Materials Science & Engineering A

journal homepage: www.elsevier.com/locate/msea

Fragmentation and mechanical performance of tailored nickel-aluminum laminate compacts

Andrew M. Marquez[a], Zezhou Li[a], Christopher H. Braithwaite[b], Timothy P. Weihs[c], Nicholas M. Krywopusk[c], David J. Gibbins[c], Marc A. Meyers[a,d,*]

[a] Materials Science and Engineering Program, University of California, San Diego, La Jolla, CA 92093-0411, USA
[b] SMF Group, Cavendish Laboratory, Cambridge CB3 0HE, UK
[c] Johns Hopkins University, Baltimore, MD 21218, USA
[d] Department of NanoEngineering, University of California, San Diego, La Jolla, CA 92093, USA

ABSTRACT

The fragmentation of materials is a complex sequence of physical processes in which the kinetic energy is converted into deformation and fracture energy. The incorporation of reactive mixtures adds a third form of energy, chemical energy. The fragmentation and mechanical performance of nickel-aluminum compacts was examined under dynamic conditions using mesostructured powder compacts in which the interfaces between the powders (having initial sizes between 355 and 500 μm) were tailored during the swaging fabrication process. Fragmentation was created in ring samples of this material through explosively driven expansion (generating velocities around 100 m/s) and analyzed through high-speed photography, laser interferometry and soft capture of fragments. Quasi-static and dynamic mechanical testing was conducted to examine the mechanical performance and to provide parameters for the constitutive description. Experimental results are compared with fragmentation theories to characterize the behavior of reactive powders based on the material's mesostructure by introducing the fracture toughness of the compacts, following the principal elements of the earlier work on tailored aluminum compacts. The fracture toughnesses, which ranged from 0.17 to 0.67 MPa $m^{1/2}$, are related to the interfacial cohesion between particles and the fragmentation is a direct consequence of these parameters. The mean fragment size is calculated using a modified form of Mott's theory and successfully compared with experimental results; it ranges from 10 μm to 40 μm. Finite element simulations on Al compacts confirm that the fragmentation increases (smaller fragment sizes) with a decrease in fracture toughness. The methodology developed here can be applied for tailoring the fragmentation of reactive munitions.

1. Introduction

Fragmentation of solids under dynamic loading has been a topic with a great deal of research, primarily for ballistic applications, where one goal is to tailor the fragment size for high-explosive projectiles. The history of fragmentation research starts with the classic studies by Mott and coworkers [1–7] in the early 1940s, beginning with the report by Mott and Linfoot [1] as part of the Allied war effort. Mott [1–7] centered his theory on the previous work of Lineau [8] who modeled fragmentation as the random geometric fracture of an infinite one-dimensional body. Mott and Linfoot [1] utilized the same random geometric fragmentation idea and applied it to a two-dimensional geometric model. Later, Grady and Kipp [9] suggested that if fragmentation can be represented by mechanism-independent statistical descriptions, then fragment mass, as opposed to fragment size, is the more fitting random variable. In addition, they suggested that the mass of the fragment was distributed over the fragment number based on a Poisson process, or binomial if the fragment number is small, paralleling the earlier developments of Lineau [8].

In our previous work, we examined the experimental results of explosive expanding ring tests of tailored mesostructured aluminum compacts [10]. By analyzing the constitutive response of each aluminum compact through quasi-static and dynamic mechanical tests, fragment sizes were predicted with a modified Mott theory that utilizes the fracture toughness of the compacts. The results demonstrated that the modified Mott theory we developed could successfully predicts the fragment sizes for most of the compacts.

In this paper, we extend the effort by which we predicted the fragment sizes of the tailored mesostructured aluminum compacts to nickel-aluminum compacts. The Ni-Al system was selected for this study

* Corresponding author at: Materials Science and Engineering Program, University of California, San Diego, 9500 Gilman Dr. #0411, La Jolla, CA 92093-0411, USA.
E-mail address: mameyers@ucsd.edu (M.A. Meyers).

https://doi.org/10.1016/j.msea.2018.04.027
Received 1 August 2017; Received in revised form 5 April 2018; Accepted 6 April 2018
Available online 07 April 2018
0921-5093/

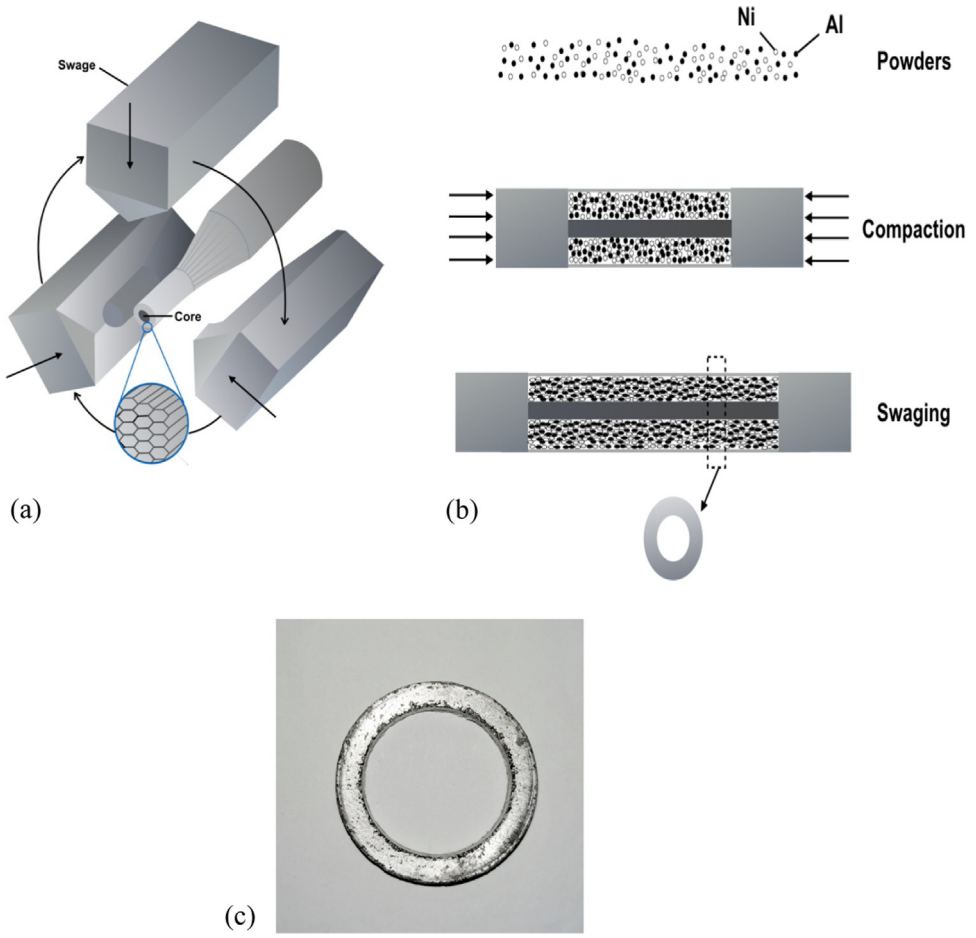

Fig. 1. Diagrams showing: (a) a depiction of the swaging method, which has three 'hammers' that converge on the specimen as shown by the arrows; after each impact the swagers are rotated; (b) the compaction and swaging procedure for powders; and (c) a photograph of a completed swaged Ni-Al ring.

because it is an optimum model system to investigate exothermic reactions initiated by dynamic events, such as ballistic impact. Also, the Ni-Al system is commonly being used as a heat source for joining components [11]. It is a reactive mixture utilized for combustion synthesis, a major technological process for the production of many intermetallics, composites and ceramics [12]. There is considerable interest in creating shell casings that react exothermically under shock-wave loading caused by detonation and during the impact of the fragments on the targets, augmenting the kinetic energy with additional exothermic chemical energy.

2. Experimental methods

2.1. Swaging

The central motivation of this research was to tailor the fragmentation response of the nickel-aluminum compacts by altering the interfacial cohesion between particles. The strength of the interface was changed through a sample processing technique called swaging, illustrated in Fig. 1(a). This is a standard forging process where a rapidly rotating die uniformly reduces the diameter of a tube or rod by cold working. The Ni-Al reactive powders were prepared by a special technique [13]. This consists of cold rolling stacks of Ni and Al sheets. This procedure ensures the establishment of intimate interfaces between the two metals and thus enables their reaction under controlled and tailored conditions. The bimetal laminates are subsequently broken and inserted into a blender, where they are cut into the desired particle size. In the present case, it is 355–500 μm. Thus, each particle is a laminate Ni-Al composite. The degree of rolling establishes the thickness of the bilayers. The Ni-Al powders were compacted into tubes of AISI 304 stainless steel in an Instron 5582, as depicted in Fig. 1(b), and then were swaged to a smaller diameter using a Fenn 5F swager. Before the compaction of the powders and swaging, tight fitting rods of Al 6061 were secured in the center of the tubes. The core diameter was set at 12.7 mm and 18.8 mm or removed to observe the effect of different degrees of compaction. As the compaction increases, it is expected that more adhesion occurs between the individual powders [14] caused by the greater degree of plastic deformation and interparticle friction. The addition of the core creates an increase in the degree of plastic deformation for a certain fraction of densification because the particles are not only brought together but also there is significantly more interparticle shear and breaking of surface oxides. The larger the central rod diameter, the greater the compaction of the powder. The rods were machined out later along with the stainless steel jackets to create hollow cylinders with 30 mm OD and 22 mm ID that were cut into 4 mm thick rings, an example of which is shown in Fig. 1(c).

2.2. Expanding ring technique

The rings described in the previous section were utilized for explosively driven fragmentation tests conducted using the experimental set-up as described by Marquez et al. [10]. This experimental setup offers high-speed photography of the ring expansion, time-resolved velocimetry of the radial expansion of the ring, and soft capture of the fragments to allow for post-fracture analysis [15]. The ring is expanded through the use of a column of explosives contained within a copper "transmitter" tube. The main charge is 0.7 g Primasheet 1000 and the detonator was Teledyne np-501. A steel cylinder coated with

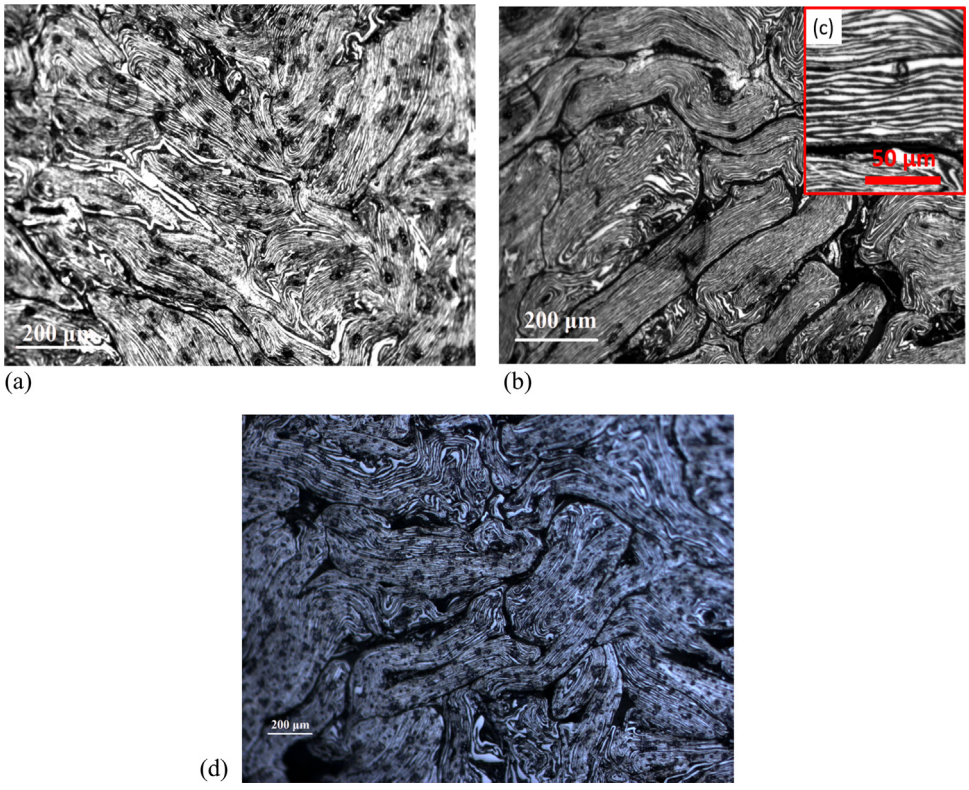

Fig. 2. Microstructures observed through optical microscopy for: (a) ~ 400 µm NiAl swaged with 18.8 mm core; (b) ~ 400 µm NiAl swaged with 12.7 mm core; (c) inset shows the lamination pattern in NiAl compacts; (d) ~ 400 µm NiAl swaged with no core.

approximately 20 mm of paraffin wax is encased around the specimen so that the fragments decelerate to a stop before impinging on the steel, eliminating the chance of secondary deformation. High-speed photography is performed parallel to the cylinder axis through the setup shown in Fig. 2(b). The radial expansion velocity of the ring is determined by a Photon Doppler Velocimetry (PDV) system [16] with the probe being a bare fiber placed approximately 3–5 mm from the ring.

2.3. Mechanical testing

Cylindrical samples with dimensions of 4 mm (length) × 3 mm (diameter) were machined from the swaged nickel-aluminum compacts. These samples were mechanically tested in a universal testing machine (Model Instron 3370) and split Hopkinson pressure bar. The samples were compressed quasi-statically with the Instron at strain rates of 10^{-2}, 10^{-3}, and 10^{-4} s^{-1}. For the dynamic testing a copper pulse-shaper with a high work-hardening rate was used to generate a long rise time and nearly square strain rate pulse [17]. Strain rates of ~ 10^{3} s^{-1} were attained through this technique.

2.4. Fragment size measurement

As described previously, the fragments from the expanding ring tests are captured in a layer of paraffin wax that is encased around the specimens. The wax is then heated in order for it to melt and leave behind the fragments from the tests to be collected for measurement and post-fracture analysis. Due to the small scale of the fragments, they were measured with imaging software. First the fragments were spread evenly over a white background. Then they were photographed and measured using the particle analysis function in the ImageJ imaging software. This enabled obtaining an average fragment size.

2.5. Fracture toughness determination

Predicting fragment sizes using the modified Mott equation developed in this study (Section 3.3.2) requires that fracture toughness values must be determined for the various conditions of swaged Ni-Al powder compacts. Thus, experiments were performed to obtain the fracture toughness values using the ASTM standard test method for linear-elastic plane-strain fracture toughness of metallic materials (ASTM E399), with some minor variations. Swaged nickel-aluminum rings were sectioned in half and a starter notch was cut in the center of the half-rings in order to create arc-shaped tension specimens (as seen in the high speed photographs in Fig. 5). Loading fixtures were constructed to allow for the application of tensile tractions without the necessity of machining loading holes in the specimens; the latter could influence the behavior of the swaged materials. The slight modification of the supports from the ones recommended in ASTM E399 is not thought to alter the effectiveness of the testing procedure significantly.

3. Results and discussion

3.1. Characterization of compacts

The various conditions of swaged Ni-Al powder compacts were characterized through density analysis, hardness testing, and optical microscopy. The percentage of densification was examined along with the degree of porosity by utilizing ASTM standard C380. The hardness testing was performed using a diamond indenter on a micro-indentation tester (LM-810, Leco corporation, MI, USA) according to the procedures in ASTM standard E384. The results of these tests are listed in Table 1. It is observed that there is a trend of increasing density percentage and decreasing apparent porosity by greater than 2% as the core size was increased. The microstructures observed through optical microscopy are shown in Fig. 2(a)–(d). The laminate nature of the individual particles is clearly seen in the inset of Fig. 2(c). The approximate thickness

Table 1
Results of density, porosity and hardness testing for the swaged Ni-Al compacts.

Compacts	NiAl (No core)	NiAl (12.7 mm core)	NiAl (18.8 mm core)
Average Density Percentage (%)	80.5 ± 0.28	84.3 ± 1.3	86.2 ± 2.1
Average apparent porosity (%)	10.4 ± 0.14	8.37 ± 1.2	6.04 ± 0.8
Hardness (GPa)	1.2 ± 0.1	1.1 ± 0.04	1.2 ± 0.1

of the bilayers is 150 μm. This is the direct result of the enhanced densification using the largest core (18.8 mm). There also appears to be a trend of less space between the particles as the core size was increased prior to swaging.

3.2. Mechanical response

There is no clear distinction between elastic and plastic regions and the curves show a gradual transition which makes the establishment of yield stress challenging. The yield stress was determined at a permanent strain of 0.002, which is obtained by a line parallel to the elastic loading. The results of the compression tests (Fig. 3(a) and (b)) showed that the 355–500 μm nickel-aluminum samples swaged with an 18.8 mm core have the highest yield stresses (~ 155 MPa), followed by the samples swaged with a 12.7 mm core (~ 150 MPa), and then the samples swaged with no core (~ 135 MPa). The high strain-rate tests of the samples were performed with the split-Hopkinson bar as mentioned previously. The dynamic yield stresses varied from 140 to 180 MPa (Fig. 3(c)) and are considerably higher than the quasi-static values. Similar to the previous study with swaged aluminum compacts [10], the order of highest dynamic yield stresses was consistent with the quasi-static results. The quasi-static and dynamic yield stresses are plotted as a function of strain rate in Fig. 3(d). The strain-rate sensitivity, m, a parameter that signifies how much the nickel-aluminum compacts flow stress and work-hardening rate may be affected by strain rate can be determined from the plot. The strain-rate sensitivity is defined as $m = \partial \ln \sigma / \partial \ln \dot{\varepsilon}$. A best fit straight line considering the average stress values for the three NiAl compacts was added to Fig. 3(d). This produces a strain-rate sensitivity of 0.024. A similar strain-rate sensitivity, 0.028, has been reported by Wei et al. [18] for Ni + Al compacts. The value is higher than that for pure aluminum (0.007) and pure nickel (0.003) from past studies [10]. Face-centered cubic (fcc) metals usually have a low strain-rate sensitivity because the flow stress is determined by cutting dislocation forests. The increase in the strain-rate sensitivity for the NiAl compacts with their laminate structure, as shown in Fig. 2(c), may be attributed to the reduction in the mean free path of dislocations. Indeed, nanocrystalline and ultrafine-grained fcc metals have a higher strain-rate sensitivity.

3.2.1. Fracture toughness results

Throughout the fracture toughness tests a high speed camera was utilized to measure the displacement of the crack mouth in place of displacement gages. The crack mouth opening displacement (CMOD) was analyzed frame by frame, as shown in Fig. 4, and compared to the force-time record in order to create a force-CMOD record as shown in Fig. 5. Then a conditional force is utilized to calculate the fracture toughness value by using the procedure detailed in ASTM E399 and the following equation:

$$K_Q = \frac{P_Q}{B\sqrt{W}}\left(3\frac{X}{W}+1.9+1.1\frac{a}{W}\right)\left[1+0.25\left(1-\frac{a}{W}\right)^2\left(1-\frac{r_1}{r_2}\right)\right]\cdot f\left(\frac{a}{W}\right) \quad (1)$$

where:

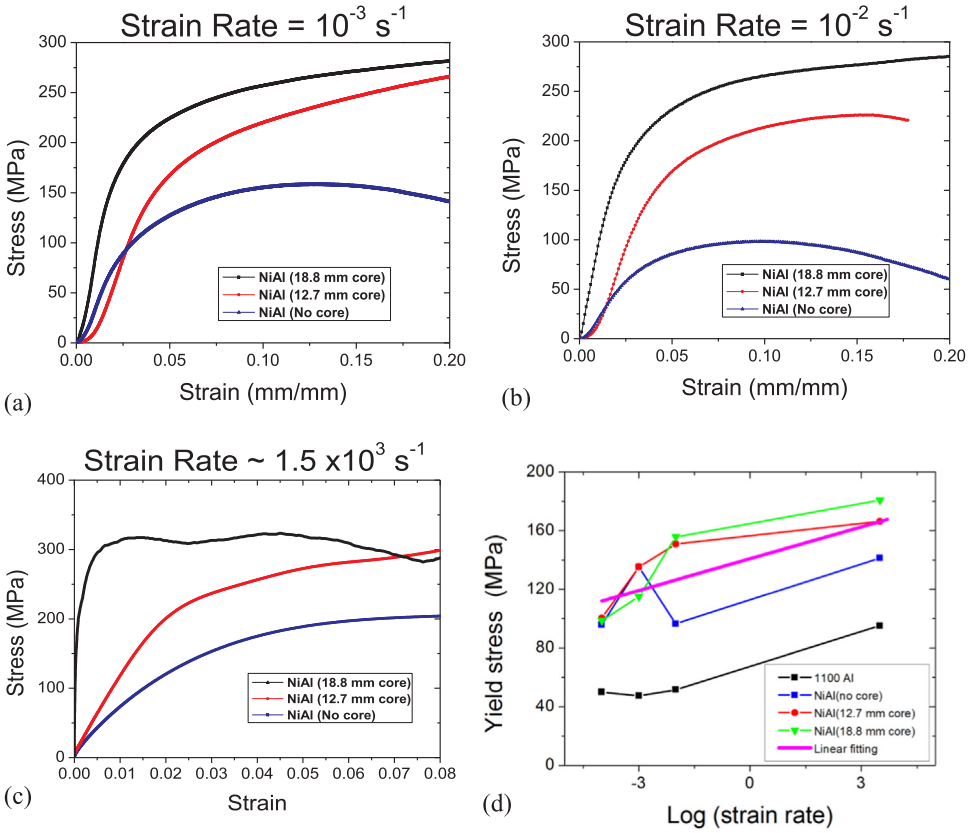

Fig. 3. Constitutive response of compacts in compression: (a) $10^{-3}\,s^{-1}$; (b) $10^{-2}\,s^{-1}$; (c) $1.5 \times 10^{3}\,s^{-1}$; (d) combined plots showing the yield stress as a function of strain rate. The straight line represents the linear fit of average stress values for the three types of NiAl compacts.

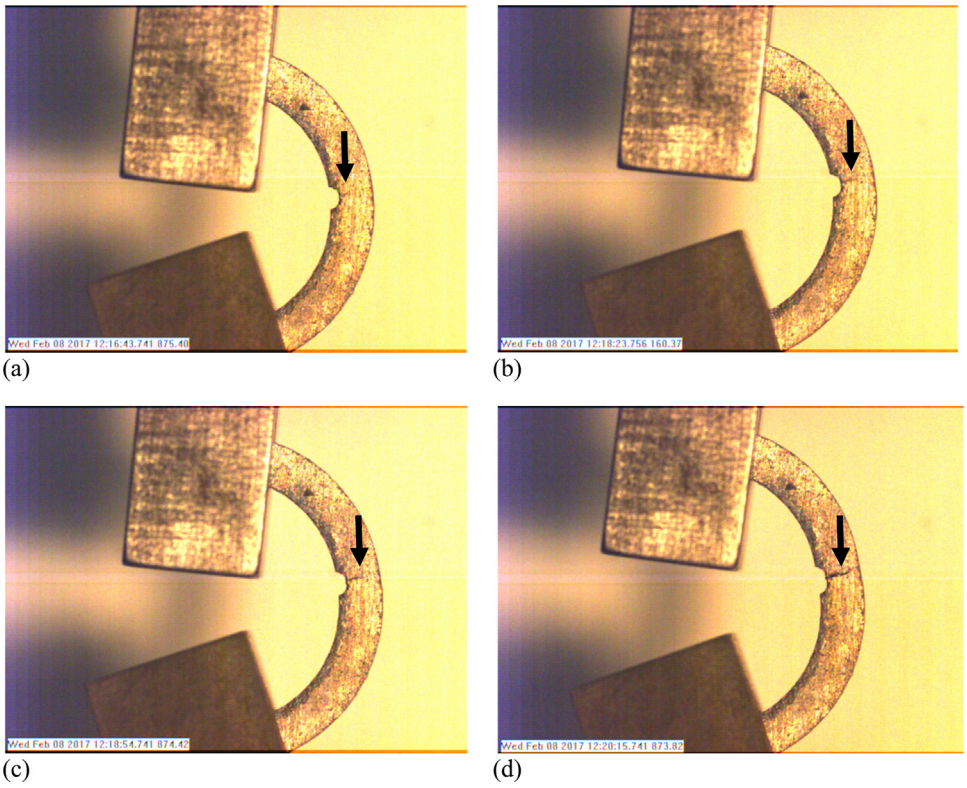

Fig. 4. Several frames from the high-speed recording of the fracture toughness test with the loading fixtures attached at the top and bottom of the specimen: (a) frame captured from the beginning of the test; (b) frame captured at the onset of fracture; (c) frame captured just before complete fracture and failure; (d) frame showing the end of the test. The crack progression is outlined by the arrows along the surface of the rings.

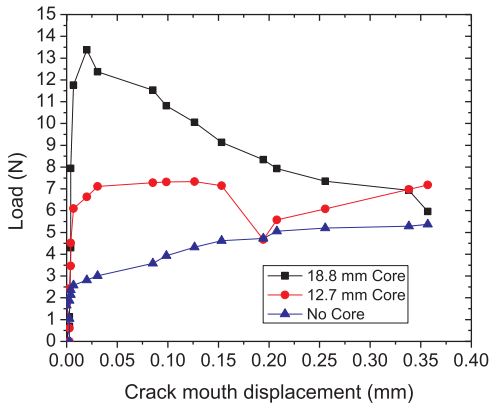

Fig. 5. Force-crack mouth opening displacement (CMOD) records from the fracture toughness tests.

$$f\left(\frac{a}{W}\right) = \frac{\sqrt{\frac{a}{W}}}{\left(1-\frac{a}{W}\right)^{3/2}}\left[3.74 - 6.30\frac{a}{W} + 6.32\left(\frac{a}{W}\right)^2 - 2.43\left(\frac{a}{W}\right)^3\right]$$

B is the specimen thickness, X is the loading offset, W is the width (depth) of the specimen, a is the crack size and r_1/r_2 is the ratio of inner-to-outer radii [19,20]. The measured fracture toughness values of the compacts are 0.17, 0.39 and 0.67 MPa $m^{1/2}$ for the specimens with no core, 12.7 mm core, and 18.8 mm core respectively. The fracture toughness increases with the amount of deformation imparted by the swaging process. These values are very low compared with bulk materials, K_{Ic} = 6 MPa $m^{1/2}$ for bulk NiAl, because of the weak interfaces that are present in the material.

3.3. Fragmentation

As previously described, recording of the fragmentation of the rings in the expanding ring experiments was conducted with a high-speed photography system set up parallel to the cylinder axis. The photographs are shown in Fig. 6. The approximate number of fragments from each experiment is shown in Table 2. The ImageJ software provides the mean fragment size, which is also given. The particles are smaller than the original powder size and this shows that fragmentation occurs both by inter- and intra-powder fracture.

3.3.1. Characterization of fracture

In order to characterize the failure morphology in the fragments of the rings, they were examined under scanning electron microscopy. The outer deformed fracture surfaces of the nickel-aluminum swaged with an 18.8 mm core (Fig. 7(a)) exhibit undulating surfaces that are typical of ductile deformation. The dimple morphology observed on the edges of these fragments is characteristic of ductile failure as well. Energy-dispersive x-ray (EDX) analysis was also performed on the fragments (Fig. 7(b) and (c)) to study the contents after the expanding ring tests. It was observed that much of the fragment was covered in carbon and oxides likely from the explosive but there was still an almost even distribution of nickel and aluminum on the portions that could be analyzed clearly. The fragments of the nickel-aluminum rings swaged with a center rod of 12.7 mm or no core at all, shown in Fig. 8(a)–(c), demonstrate features that are indicative of a brittle failure such as interparticle separation. The dissimilarity in the fracture surfaces indicates how a brittle failure induces the production of more fragments. The fracture surfaces in the toughness specimens were observed and shown in Fig. 9(a)–(c). The nickel-aluminum swaged with an 18.8 mm core shows a high resistance to intergranular fracture in fracture toughness tests. Fig. 9(a) shows larger fracture particles, while brittle intergranular fracture surfaces are observed in Fig. 9(b) and (c) for NiAl compacts swaged with a 12.7 mm core and no core.

3.3.2. Prediction of mean fragment sizes

In 1943 Mott and Linfoot proposed a fundamental theory for the prediction of mean fragment sizes based on an energy balance [1] that was similar to the Griffith theory for crack propagation [21]. Many further complex analyses have been developed since then but the

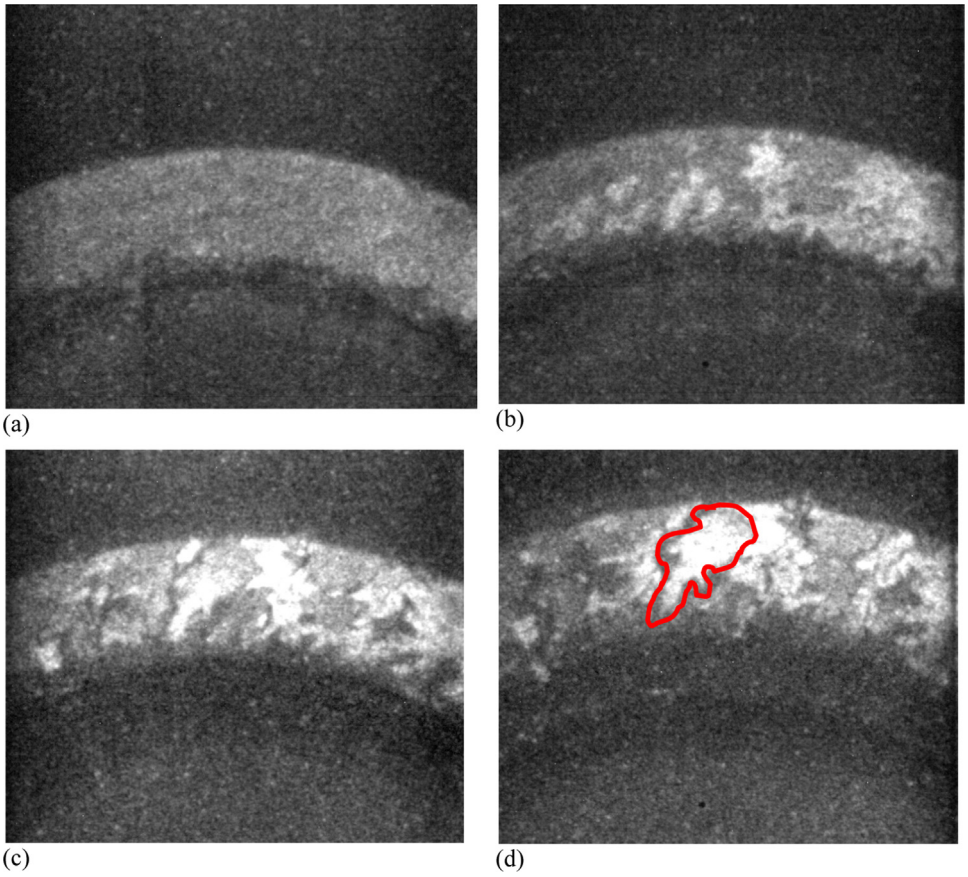

Fig. 6. Sequence showing initiation of cracking and fragmentation in an expanding ring test of the swaged NiAl compact. One of the largest fragments that resulted from this test is outlined in the final photograph (d) of the sequence.

Table 2
Number of fragments from expanding ring tests of swaged Ni-Al compacts.

Compacts	NiAl (No core)	NiAl (12.7 mm core)	NiAl (18.8 mm core)
Fragment number	~ 4000	~ 2500	~ 1000
Experimental mean fragment size (μm)	10	20	40

original analysis by Mott will be used for our purpose as it is the most basic analysis to expand upon. Thus, some modification of the Mott equation [22–26] will be presented. The derivation was presented in integral form in the earlier study of mesostructured aluminum compacts [10], so only the essential derivation of the Mott-Linfoot equation is given here. Fig. 10 is a schematic illustration of a segment of size a just prior to fragmentation. The radial velocity is V_r. As a result of the ring expanding the extremities of the chosen differential element move apart and we can define a tangential velocity V_t, with respect to prior to fragmentation. The arc has an angle α, thus we have, after the radius has expanded to $r + dr$:

$$V_r = \frac{dr}{dt} \tag{2}$$

$$V_t = \frac{da}{2dt} \tag{3}$$

Thus:

$$V_t = \frac{daV_r}{2dr} \tag{4}$$

However:

$$a = \alpha r \quad and \quad da = \alpha dr \tag{5}$$

Substituting Eq. (5) into Eq. (4):

$$V_t = \frac{\alpha V_r}{2} \tag{6}$$

The basic assumption made by Mott [1] was that the kinetic energy was converted into the energy to generate two cracks at the extremities of the fragment. Due to the number of cracks being equal to the number of fragments, only one crack has to be considered per fragment. We replace Mott and Linfoot's energy per unit area required to form a crack by the energy release rate, $G = \frac{K_{Ic}^2}{E}$, which considers the toughness of the material. Therefore, the fragment size can be found:

$$a = \left(\frac{24r^2K_{Ic}^2}{V_r^2\rho E}\right)^{1/3} \tag{7}$$

The introduction of the strain energy (a potential energy term) into the Mott theory can be simply made through the addition of:

$$E_e = \left(\frac{1}{2}\sigma_y\varepsilon\right)at \tag{8}$$

Through the use of Hooke's law, the elastic deformation energy is obtained:

$$E_e = \frac{\sigma_y^2}{2E}at \tag{9}$$

Incorporating the potential (strain) energy and fracture toughness leads to a more accurate prediction of fragment size:

$$a^3 + \frac{24r^2\sigma_y^2}{2E\rho V_r^2}a - \frac{24r^2K_{Ic}^2}{E\rho V_r^2} = 0 \tag{10}$$

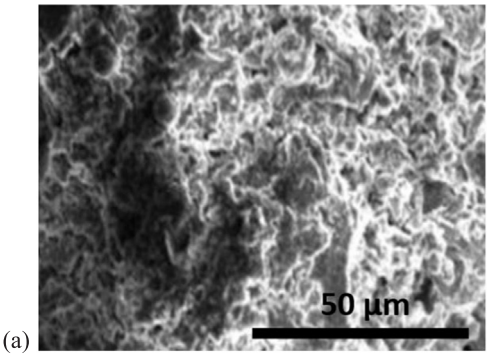

(a)

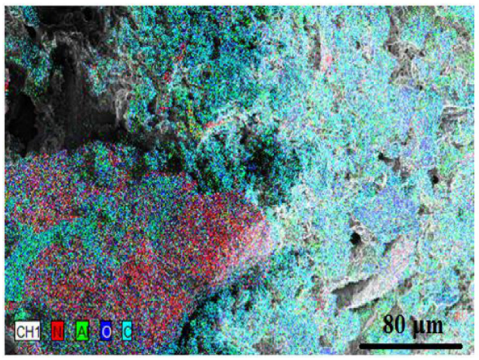

(b)

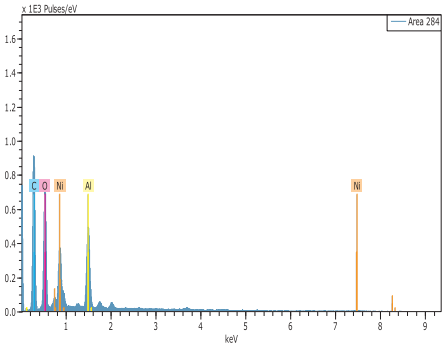

(c)

Fig. 7. (a) Fracture surfaces from expanding ring tests of the swaged NiAl compact made with 18.8 mm core, containing ductile dimples. The result of EDX analysis of a small portion of the fragment is shown in (b) and (c).

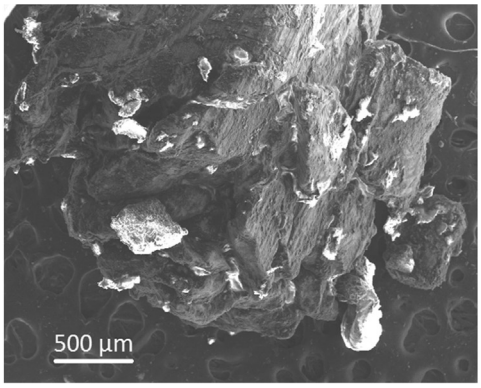

(a)

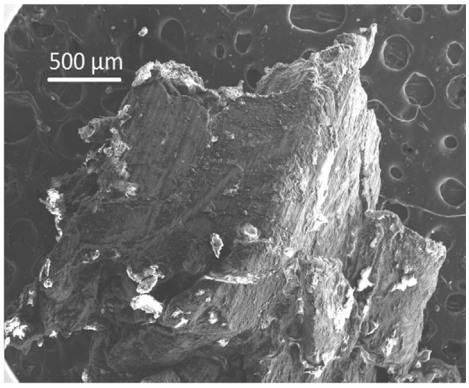

(b)

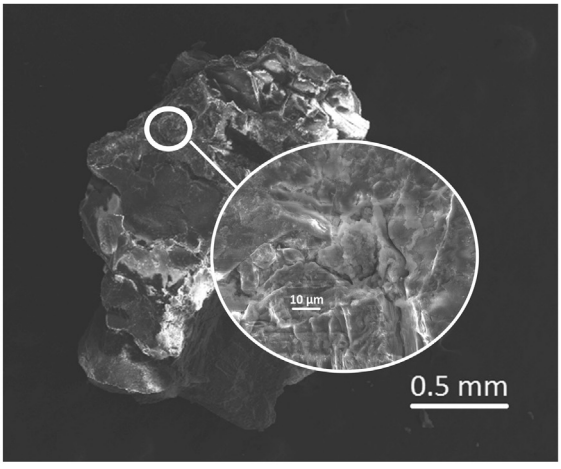

(c)

Fig. 8. Fracture surfaces from expanding ring tests of the swaged NiAl compact made with a 12.7 mm core (a, b). Note the interparticle cracking on these surfaces that are indicative of brittle failure, specifically in the high magnification inset of the fragment from the compact swaged with no core (c).

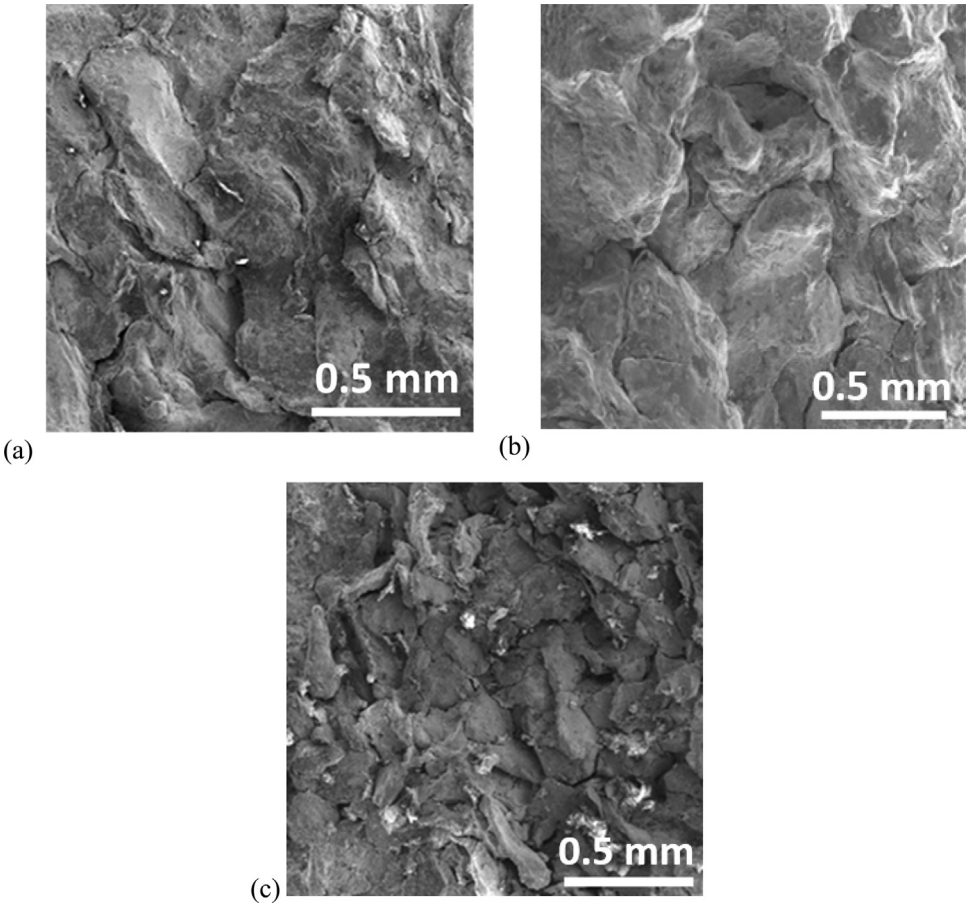

Fig. 9. Fracture surfaces from fracture toughness tests of the swaged NiAl compacts: (a) swaged with 18.8 mm core; (b) swaged with 12.7 mm core; (c) swaged with no core.

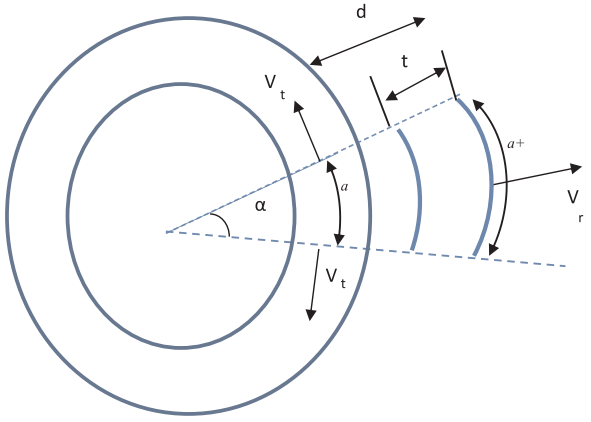

Fig. 10. Schematic drawing of expansion fragmentation process following Mott's theory using a segment of ring with parameters used in the derivation. Two velocities are considered: a radial velocity V_r and a tangential velocity V_t. The latter accounts for the increase in lateral dimensions of the segment as expansion takes place.

Eq. (10) indicates that, for a fixed velocity, the fragment size is a function of both the strength and fracture toughness. The solution of this incomplete third order equation $a^3 + pa + q = 0$ gives the predicted fragment size in the remaining real root as solved for in an earlier study [10].

This is the result of the modification to the Mott fragmentation theory. Once a fracture toughness value is obtained it can be used with other experimentally determined values in Eq. (10) to predict a mean fragment size. The calculated fracture toughness values and experimentally measured mean fragment sizes for each of the compacts are presented in Table 3.

Table 3
Measured fracture toughness values and predicted and measured mean fragment sizes for the different compacts.

Compacts	~ 400 μm NiAl (No core)	~ 400 μm NiAl (12.7 mm core)	~ 400 μm NiAl (18.8 mm core)
Fracture toughness value (MPa $m^{1/2}$)	0.17	0.39	0.67
Predicted mean fragment size (μm)	6	14	39

Experimentally measured mean fragment sizes of the swaged nickel-aluminum are compared to the predicted values based on measured fracture toughness using the modified Mott theory (Eq. (10)) in Fig. 11. The radius of ring $r = 12 \times 10^{-3}$ m, the radius velocity $v = 100$ m/s, the average Young's modulus $E_{average} = 135$ GPa and the average density $\rho_{average} = 5.9 \times 10^3$ kg/m^3 for Eq. (10) are used here. The predicted mean fragment sizes are given by the blue, green and red lines for yield stresses of 135, 150, and 155 MPa, respectively; the experimentally measured fragment sizes are given by the black line. These values correlate, approximately, with the compressive strength results at 1.5×10^3 s^{-1}. The yield stress for each condition is marked in the plot. The experimentally measured mean fragment sizes correlate reasonably well with the predictions, being only slightly higher than the predicted fragment for yield stress of 150 MPa. This could be due to the fact that some fractures may not have opened completely, therefore leading to

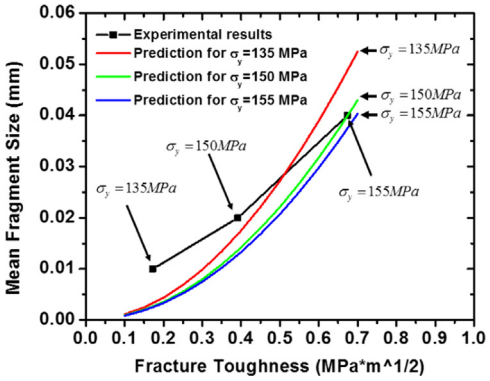

Fig. 11. Experimentally measured mean fragment sizes (black line) of the swaged nickel-aluminum compared to the predictions for fragment sizes based on fracture toughness with the modified Mott theory within a range of yield stresses typical to the swaged nickel-aluminum. The fragment size is dependent on both fracture toughness and yield stress, as shown by the three curves for 135, 150 and 155 MPa. The yield stresses of the experimental conditions are noted above each point.

two or more fragments being counted as one. Therefore, the modified Mott theory is shown to be able to predict fragment sizes for materials within ranges of yield stresses typical to that material for not only swaged aluminum rings like the previous study performed with this same process, but also with mixtures of aluminum such as the tailored swaged nickel-aluminum compacts.

3.3.3. Simulation

Finite element simulations were conducted to compare the experiments with predictions. The results of the numerical simulation of fracture in the expanding ring tests of Al compacts are summarized in Fig. 12. The classical Johnson-Cook [23] constitutive equation was used to describe the mechanical behavior of the compacts:

$$\sigma = (A + B\bar{\varepsilon}_p^{n})(1 + C \ln \dot{\varepsilon}^{*}) \quad (11)$$

where A is the yield stress, B is the hardening modulus, C is the strain rate constant, $\bar{\varepsilon}_p^{n}$ is the effective plastic strain and $\dot{\varepsilon}^{*}$ is the normalized effective strain rate. The parameters for the Al rings in the simulations, shown in Table 4, were taken from the experimental results of the quasi-static and dynamic testing [10].

The simulation of the 40 μm Al swaged powder ring (Fig. 12(a)) depicts the fracture in two positions with a similar pattern captured by the high-speed camera from the expanding ring tests. When considering the quarter symmetry of the simulation mirrored over the entire ring, it would be expected to produce 8 fragments, as were collected from the experiment. The pattern of fracture observed in the simulation of the 400 μm Al swaged powder ring (Fig. 12(b)) was also similar to that seen in the experiment. When the quarter symmetry of this simulation is considered over the entire ring, approximately 32 fragments are predicted. However, as seen in the simulation, some of the fragments were considerably small such that they could have reduced to powder by the end of the explosive experiment. The brittle fracture observed in the high speed photographs of the 100 μm Al swaged powder rings was also demonstrated by the simulation (Fig. 12(c) and (d)). These simulations demonstrate that the a low facture toughness value leads to more fragmentation in the expanding ring tests. The ductile 40 μm and 400 μm Al compacts show larger fragment sizes as presented in the simulations in Fig. 12. This also agrees well with the finding that the NiAl compact (swaged with 18.8 mm core), obtaining higher fracture toughness, has a more ductile failure (Fig. 7). Similarly, it exhibits larger fragment sizes during expanding ring tests as measured in Table 3 and as predicted in Fig. 11.

4. Conclusions

Nickel-aluminum compacts manufactured by swaging to have varying interfacial strengths were subjected to fragmentation. The strength of the interfaces between particles was tailored by the amount

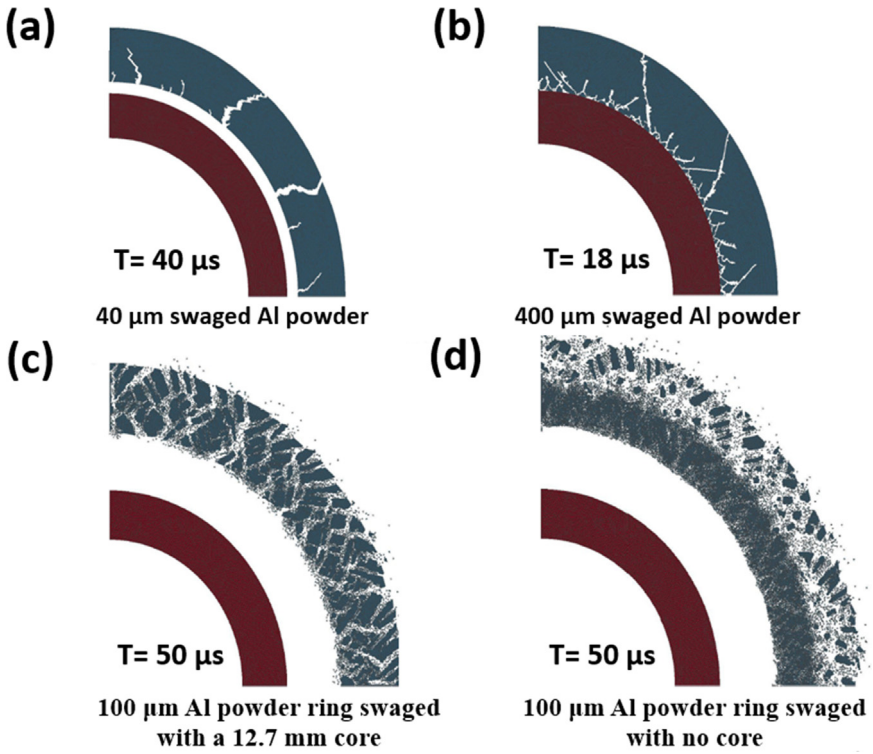

Fig. 12. Fracture (at different times) of expanding rings in FEM simulation for (a) 40 μm swaged Al powder; (b) 400 μm swaged Al powder; (c) 100 μm swaged Al powder with 12.7 mm core; (d) 100 μm swaged Al powder with no core. Note the differences in fragmentation pattern, governed by the fracture toughness.

Table 4
Parameters for simulations of fracture in the expanding ring tests in Al compacts.

Compacts	40 μm Al (12.7 mm core)	100 μm Al (No core)	100 μm Al (12.7 mm core)	400 μm Al (18.8 mm core)
Density	2.69 g/cm^3	2.69 g/cm^3	2.69 g/cm^3	2.67 g/cm^3
Young's modulus	0.197 Mbar	0.066 Mbar	0.131 Mbar	0.137 Mbar
Poisson's ratio	0.345	0.345	0.345	0.345
Yield stress (A)	8.40 × 10^{-4} Mbar	7.00 × 10^{-4} Mbar	6.00 × 10^{-4} Mbar	1.20 × 10^{-3} Mbar
Hardening modulus (B)	6.97 × 10^{-3} Mbar	3.32 × 10^{-4} Mbar	2.48 × 10^{-3} Mbar	2.40 × 10^{-3} Mbar
Strain rate constant (C)	0.007023	0.006516	0.007902	0.008517
Strain exponent (n)	1.320	0.123	0.835	0.800
Plastic strain of failure (PSFAIL)	0.220900	0.013916	0.029307	0.079440
Strain rate of reference (EPS0)	1 × 10^{-8} s^{-1}	1 × 10^{-8} s^{-1}	1 × 10^{-8} s^{-1}	1 × 10^{-8} s^{-1}

of plastic work imparted by the plastic deformation in swaging. In order to examine the mechanical performance of these compacts, quasi-static and dynamic compression tests were carried out. It was discovered that the degree of compaction had a significant effect on constitutive response of the swaged nickel-aluminum. By performing the ASTM standard test method for linear-elastic plane-strain fracture toughness of metallic materials (ASTM E399) with some minor variations, fracture toughness values for the modified Mott equation were found. Additionally, expanding ring tests were performed with the compacts to study the fragmentation behavior of the compacts. Through scanning electron microscopy the fracture response of the swaged Ni-Al rings was examined. The Ni-Al rings swaged with an 18.8 mm core revealed ductile fracture behavior while the Ni-Al rings swaged with a 12.7 mm core or without any core contained brittle material fracture features. Apparently, more ductile Ni-Al rings swaged with an 18.8 mm core produce much fewer fragments than the more brittle Ni-Al rings swaged under different conditions. EDX analysis was also conducted on the fragments to examine their elemental composition. The results showed an almost even distribution of nickel and aluminum on the sections of the fragment that could be examined clearly without debris from the Primasheet 1000 explosive.

Mean fragment size predictions were calculated with a modified Mott equation similar to the Grady-Kipp theory. The experimentally measured mean fragment sizes were found to be close to the predictions of fragment size based on fracture toughness by the modified Mott theory. This indicates that the modified Mott theory predicts the fragment sizes for the swaged Ni-Al rings just as well as it did in the previous study performed under these conditions with swaged aluminum rings [10]. Thus, the modified Mott analysis incorporating fracture toughness is a good predictor of fragment sizes. Finite element simulations on a simplified model material (pure aluminum) predict different fragmentation patterns that correlate well with the experimental results and modified Mott analysis: as the toughness increases, so do the fragment sizes.

Acknowledgements

The authors gratefully acknowledge financial support provided by ONR/MURI Grant No. N00014-07-1-0740 (Program Officer Dr. Clifford Bedford). We acknowledge Prof. V. F. Nesterenko for the use of the high-speed camera. Prof. O. Graeve and Mr. Keyur Karandikar helped to conduct the density and porosity measurements, and their input is greatly appreciated. Also, we would like to acknowledge Tarah N. Sullivan for her assistance with the illustrations. Discussions with Dr. S. Walley at Cavendish Laboratory are gratefully acknowledged.

References

[1] N.F. Mott, E.H. Linfoot, A Theory of Fragmentation, Ministry of Supply, AC 3348, 1943.
[2] N.F. Mott, Fragmentation of H.E. Shells: A Theoretical Formula for the Distribution of Weights of Fragments, Ministry of Supply, AC3642, 1943.
[3] N.F. Mott, A Theory of the Fragmentation of Shells and Bombs, Ministry of Supply, AC4035, 1943.
[4] N.F. Mott, Fragmentation of Shell Casings and the Theory of Rupture in Metals, Ministry of Supply, AC4613, 1943.
[5] N.F. Mott, A Theory of Fragmentation: Application to Wire Wound Bombs Such as the American 20 lb, F, Ministry of Supply, AC6338, 1944.
[6] N.F. Mott, J.H. Wilkinson, T.H. Wise, Fragmentation of Service Projectiles, Ministry of Supply, AC6338, 1944.
[7] N.F. Mott, Fragmentation of shell cases, Proc. R. Soc. Lond. 189 (1947) 300–308.
[8] C.C. Lineau, Random fracture of a brittle solid, J. Frankl. Inst. 221 (1936) 485–494.
[9] D.E. Grady, M.E. Kipp, Geometric statistics and dynamic fragmentation, J. Appl. Phys. 58 (1985) 1210–1222.
[10] A.M. Marquez, C.H. Braithwaite, T.P. Weihs, N.M. Krywopusk, D.J. Gibbins, K.S. Vecchio, M.A. Meyers, Fragmentation and constitutive response of tailored mesostructured aluminum compacts, J. Appl. Phys. 119 (2016) 145903.
[11] A.J. Swiston, T.C. Hufnagel, T.P. Weihs, Joining bulk metallic glass using reactive multilayer foils, Scr. Mater. 48 (2003) 1575–1580.
[12] N.N. Thadhani, Shock-induced chemical reactions and synthesis of materials, Prog. Mater. Sci. 37 (1993) 117–226.
[13] A.K. Stover, N.M. Krywopusk, J.D. Gibbins, T.P. Weihs, Mechanical fabrication of reactive metal laminate powders, J. Mater. Sci. 49 (2014) 5821–5830.
[14] R.Y. Yang, A.B. Yu, S.K. Choi, M.S. Coates, H.K. Chan, Agglomeration of fine particles subjected to centripetal compaction, Powder Technol. 184 (2008) 122–129.
[15] J.D. Gibbins, A.K. Stover, N.M. Krywopusk, K. Woll, T.P. Weihs, Properties of reactive Al:Ni compacts fabricated by radial forging of elemental and alloy powders, Combust. Flame 162 (2015) 4408–4416.
[16] C. Braithwaite, B. Aydelotte, A. Collins, N. Thadhani, D. Williamson, Comparing CTH simulations and experiments on explosively loaded rings, AIP Conf. Proc., 1426, 2012, pp. 1049–1052.
[17] K.S. Vecchio, F.C. Jiang, Improved pulse shaping to achieve constant strain rate and stress equilibrium in split-Hopkinson pressure bar testing, Metall. Mater. Trans. A 38 (2007) 2655–2665.
[18] C.T. Wei, E. Vitali, F. Jiang, S.W. Du, D.J. Benson, K.S. Vecchio, N.N. Thadhani, M.A. Meyers, Quasi-static and dynamic response of explosively consolidated metal–aluminum powder mixtures, Acta Mater. 60 (2012) 1418–1432.
[19] V. Nesterenko, P. Chiu, C. Braithwaite, A. Collins, D. Williamson, K. Olney, D. Benson, F. McKenzie, Dynamic behavior of particulate/porous energetic materials, AIP Conf. Proc., 1426, 2012, pp. 533–538.
[20] J.A. Kapp, J.C. Newman, J.H. Underwood Jr., A wide range stress intensity factor expression for the C-shaped specimen, J. Test. Eval. 8 (1980) 314–317.
[21] A.A. Griffith, The phenomena of rupture and flow in solids, Philos. Trans. R. Soc. A 221 (1921) 163–198.
[22] D. Grady, D.A. Benson, Fragmentation of metal rings by electromagnetic loading, Exp. Mech. 23 (1983) 393–400.
[23] G.R. Johnson, W.H. Cook, Fracture characteristics of three metals subjected to various strains, strain rates, temperatures and pressures, Eng. Fract. Mech. 21 (1985) 31–48.
[24] D.E. Grady, M.L. Olsen, A statistics and energy based theory of dynamic fragmentation, J. Impact Eng. 29 (2003) 293–306.
[25] E. Vitali, C.-T. Wei, D.J. Benson, M.A. Meyers, Effects of geometry and intermetallic bonding on the mechanical response, spalling and fragmentation of Ni-Al laminates, Acta Mater. 59 (2011) 5869–5880.
[26] R. Ames, in: A. Gash, N. Thadhani, W. Wilson, R. Armstrong, Z. Munir (Eds.) MRS Symp. Proc., vol. 896, Pittsburgh, PA, 2006.